Mechatronics 102 (2024) 103230

Contents lists available at ScienceDirect

Mechatronics

journal homepage: www.elsevier.com/locate/mechatronics

VARISA - A VARIable Stiffness soft robotics Arm based on inverse pneumatic actuators and differential drive fiber jamming ☆

Luca Arleo, Matteo Cianchetti *

The BioRobotics Institute, Scuola Superiore Sant'Anna, Pontedera, Italy
Department of Excellence and AI, Scuola Superiore Sant'Anna, Pisa, Italy

ARTICLE INFO

Keywords:
Fiber jamming
Variable stiffness
Modular arm
Soft robotic manipulator

ABSTRACT

Variable stiffness technologies are promising to fill the existing gap between the capabilities of robots based on soft materials and real-case applications, which may require high stiffness in specific working phases or conditions. Among these technologies, jamming transition emerged as a suitable option for devices that are intended to experience large deformations. Building upon the first version of the already introduced variable stiffness linear actuator (based on the combination of inverse pneumatic artificial muscles, fiber jamming, and positive pressure jamming), here we present the design of the VARISA, a novel multidirectional modular soft arm with tuneable stiffness. A tailored fabrication process, considered also in the design choices, is reported. Both the single module, made of three actuators, and the arm, which consists of two modules connected in series, were tested to assess deformability and variable stiffness capabilities. VARISA is 45 mm in diameter and 285 mm in length and it reached 100 mm of elongation and 82 degrees of maximum bending angle, covering a 300 mm wide workspace. Moreover, it achieved a stiffness variation close to one order of magnitude (a maximum stiffness ratio of 9.57) and, in particular, the possibility to tune the absolute stiffness between 0.06 and 0.52 N/mm in bent configuration.

1. Introduction

Soft Robotics went through substantial growth in the past decade, introducing enabling technologies and new basic robotic abilities. However, nowadays, the research community is converging on the need to fill the existing gap between research achievements and real application scenario requirements [1]. The adoption of soft materials and compliant structures in designing slender devices, such as robotic arms and endoscopes, guarantees intrinsic safe human–robot interaction. However, high compliance severely limits the possibility of exerting force on the surroundings. Therefore, a trade-off is usually required between safety and the capability to execute tasks. In this framework, variable stiffness (VS) technologies emerged as enabling technologies for soft robots [2]. Indeed, the on-demand variation of the stiffness allows researchers to bypass this trade-off: robotic arms can preserve their safety in the soft state, while the stiff state can be activated to change local mechanical properties when required. Therefore, VS technologies are of major importance in the quest for meeting the requirements of real applications.

This is true not only in the field of soft robotics. Robotic arms made of stiff materials with links and joints, already tackled the VS topic. The most adopted approach consisted in tuning the stiffness of the joints through springs and leverages of variable lengths [3–5]. The adoption of magneto-rheological fluids was also proposed for the same purpose [6]. More recently, alternative approaches based on the stiffness variability of the links and on different actuation principles were presented [7–9]. In the development of soft robotics arms instead, the VS capability pertains to the entire deformable structure. Different approaches are possible since several actuation principles are available both to achieve deformability and VS, and all of them bring specific drawbacks. However, the employment of some technologies makes the limitations emerge and shows how the VS implementation is non-trivial.

The stiffness ratio R is the most common evaluation parameter in a comparative analysis and it is defined as the ratio between the stiffness in the stiff and the soft state. Usually, this value is referred to a very common load condition, that for slender structures like arms and endoscopes, is represented by bending. The employment of actuators in antagonistic arrangements was exploited on large scales with very good dexterity performances. Although the payload of these devices was found to reach 5.5 N, the stiffness variation was limited ($R < 4$)

☆ This paper was recommended for publication by Associate Editor Kam K. Leang.

* Corresponding author at: The BioRobotics Institute, Scuola Superiore Sant'Anna, Pontedera, Italy.
E-mail address: m.cianchetti@santannapisa.it (M. Cianchetti).

https://doi.org/10.1016/j.mechatronics.2024.103230
Received 14 July 2023; Received in revised form 19 April 2024; Accepted 5 July 2024
Available online 23 July 2024

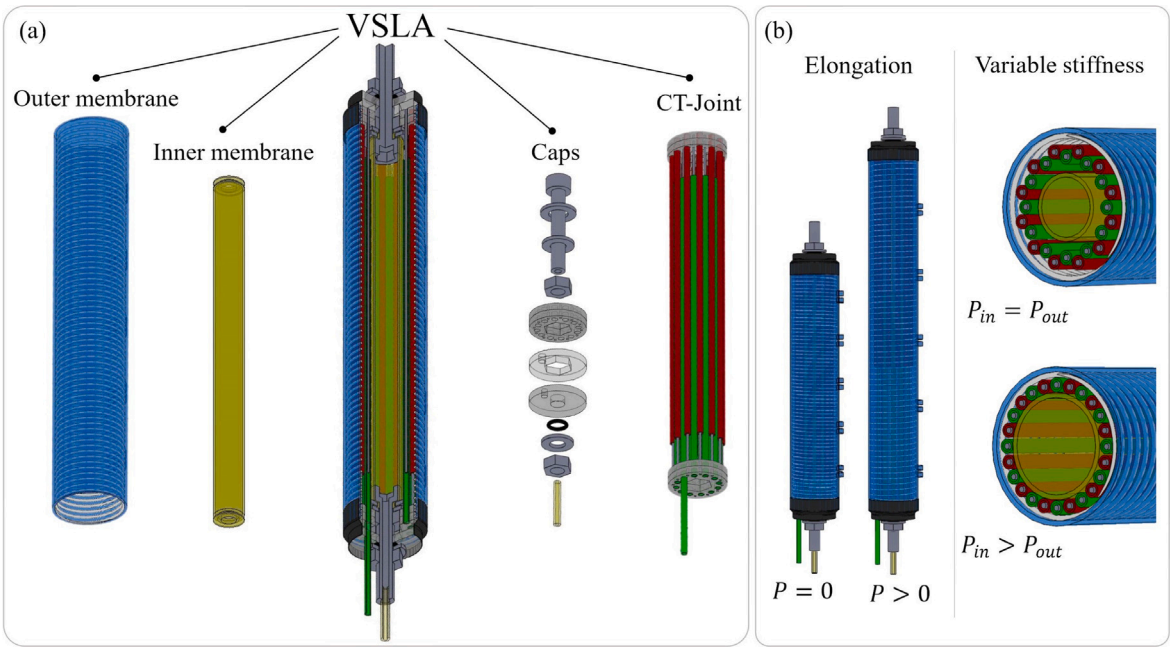

Fig. 1. (a) Design of the actuator and of its components with the exploded view of the top cap; (b) working principle: a pressure increase in both inner and outer chamber brings to elongation, while a subsequent increase in the differential pressure between the two activates the fiber jamming.

and the control became very complex [10–12]. The same applies to cable-driven robots controlled to drive both the deformation and the stiffness [13].

Temperature control-oriented methods, based on the adoption of low melting point alloys [14,15] rather than materials with low glass transition temperatures [16,17], allow to achieve values of R up to 22. However, transition times in the order of 10–100 s were reported, especially for the cooling phase. Of course, this aspect limits the applicability of these solutions in several applications. The variable stiffness performances of magnetorheological fluids-based devices were also investigated. Although this technology enabled almost real-time control with immediate transition times, the reported values of R are usually lower, reaching values between 1.7 and 4 [18,19]. Jamming transition based devices represent a trade off, showing very fast transition times (on the order of 0.01–0.1 s) and intermediate values of R. Granular jamming was adopted for endoscopes like STIFF-flop [20,21] and proposed for manipulators [22–26]. In these cases, R was between 1.6 and 5.5. In addition, the granular nature of the filler does not guarantee stable performances in case of large deflections and elongations, therefore the workspace was limited in comparison with the arm length. Xie et al. recently introduced a chain-mail based variable stiffness module capable to achieve stiffness ratios in the range 1.6–3.7, therefore in line with granular jamming based devices [27]. Layer jamming based devices were designed to overcome this issue. Very good VS performances and dexterity were achieved by Kim et al. [28], who developed a manipulator based on a jamming system made of helicoidally arranged layers. In this work, R is not reported, but the authors showed a remarkable capability of 2 N of payload in stiff state with a device whose aspect ratio (length over diameter) is equal to 19. Subsequent works adopted layer jamming and reported R equal to 4 [29] and 16.6 [30]. Although layer jamming demonstrated to be promising for small-scale devices like endoscopes, the same approach can bring buckling issues on higher scales, thus it is not a suitable candidate for manipulators capable of large deflections.

In this context, we recently introduced the variable stiffness linear actuator (VSLA) that combined IPAM (Inverse Pneumatic Artificial Muscle), Fiber Jamming and differential pressure control [31]. The VSLA in this first version showed good performances with R equal to 5.1, 13.5 and 21.3 at 0, 20 and 40% of elongation, respectively. From the beginning, the VSLA was devised to represent the fundamental basic unit of an entire VS modular arm. However, its actual definition required an almost completely re-design of some components to ensure higher reliability, modularity, and faster and easier fabrication.

In this work, we start presenting the VSLA evolution, with all the required modifications and improvements. Then, we introduce the VARISA capable of elongation, bending in multiple directions and stiffness tuning when required. Both the actuator and the arm design are driven by an optimization model which involves the main geometric parameters.

In the next section, the design of the arm is shown together with the fabrication of its main components. The characterization protocol is then reported in Section 2. In Section 3, we show and discuss the results of the characterization tests. The Conclusions end the document with a comparison of the results against the most representative state-of-the-art values and with considerations on the applicability of the arm.

2. Materials and methods

2.1. Design of the actuators

The main components of the actuators are CT-joint (Comb Type joint), inner and outer membranes, and caps (shown in Fig. 1(a)), as in [31]. The working principle is shown in Fig. 1(b): since the outer chamber cannot expand radially, when P1 = P2 the actuator elongates (IPAM behavior), while when P1>P2 the fibers are displaced and packed between the two chambers, so the stiffness increases (fiber jamming). The design of the actuator was optimized using the model reported in the supplementary material, whose MATLAB code is provided. The resulting size is 17.5 × 125 mm, with an active length of 100 mm, and the weight of the actuator is 36.5 g. Moreover, in comparison with the previous version, several improvements were done.

The CT-joint architecture includes 24 fibers coupled with the same number of guides so that the reciprocal position of the fibers is preserved while both elongation and bending are permitted. In particular, 2 mm PTFE pipes that provide optimal stability during displacements are used as fibers. From preliminary experiments we obtained that the

friction of PTFE with cotton and silicone was higher than expected, we also tested different surface treatments but no significant difference was found. As in the first VSLA, nickel wound steel strings (Ernie Ball, Inc.) with outer diameter 0.67 mm are used as guides. In addition, a longer fiber is directly used as a connection for the outer chamber pressure signal. At rest condition, the fibers and the guides are coupled for 85 mm in length in the central region, while 7.5 mm are left free at both ends.

The caps were completely redesigned so that air tightness, and speed and ease of fabrication were significantly improved. They consist of several components which can be divided into two groups: inner pneumatic connections and plates. The first group consists of four components: an M4 screw, a small and a larger washer and an M4 nut. The inner membrane, which is a 0.3 mm thick latex balloon, is inserted between the two washers and blocked through the nut. The same solution is adopted on both end and top caps. The only difference is represented by a 2 mm hole drilled in the screw of the top cap, in which a pipe of equal diameter is inserted to provide pressure to the inner chamber. The final result is similar to how standard threaded pneumatic connections work. However, using metric screws and washers as shown it is possible to adapt the size of the interface to very different diameters of the inner chamber. The second group consists of plates that are made of stacks of four 2 mm thick plexiglass discs. The first two discs (lv. 1 and 2) are shaped with a central hexagonal seat for the nuts of the inner pneumatic connections and circular seats for fibers and guides of the CT-Joint. The third disc (lv. 3) shows the hexagonal seat and a circular hole for the passage of the outer chamber pressure input. The fourth disc (lv.4) shows a circular hole for the passage of the inner pneumatic connection screw and the hole for the outer chamber pressure input. An additional nut and a small washer are screwed on the inner pneumatic connection screw to fix the components of the caps together. The addition of an O-Ring between the washer and the fourth disc ensures air tightness.

The in-extensible thread of the outer chamber is inside the silicone wall so that the helix pitch is fully restored. This chamber is fixed to the external surface of the plates using insulating tape, which ensures air tightness. In Section 2.3 the tailored fabrication process implemented to obtain these components is shown.

2.2. VARISA design

Similarly to previous soft manipulators, the arm presents a modular design [10,32]. From preliminary studies, we experienced how increasing the number of modules connected in series, the contribution to the overall deformation of the module connected to the frame greatly reduces. In particular, using modules of equal size, with three modules this effect is already substantial, making the adoption of a greater number of modules useless. Therefore we adopted an architecture composed of two equal modules, the proximal and the distal module. Each module is made of 3 actuators placed at 120 deg from each other (Fig. 2(a)). When actuators are inflated with equal pressure the module elongates, while bending is achievable with differences in the pressure inputs.

The module size can be simplified as a triangular section with 46 mm side, and its length is 135 mm. The total weight is 126 g. The design of the modules was also optimized through the model reported in the supplementary material. This optimization study supported the choice of setting the outer radius of the active part of the modules equal to 22.5 mm (the whole module is enclosed in a circle of radius 25 mm) and in the centres of the actuators positioned 13.75 mm far from the centre of the module. Moreover, independently of the actual size, thanks to the peculiar characteristics of the VSLAs, the optimization of their arrangement translates into optimal performances for the overall arm. Indeed, VS arms in which actuators are decoupled usually show either actuators appointed to deformation in the centre and stiffening elements on the external edge or the opposite. In the first case VS ability is more effective, while the capability to exert forces during motion is optimized in the second case. Therefore, decoupled solutions require a trade-off. By incorporating both VS and deformation functions in a single component, such as in our VSLA, the VARISA design here introduced does not require any trade-off.

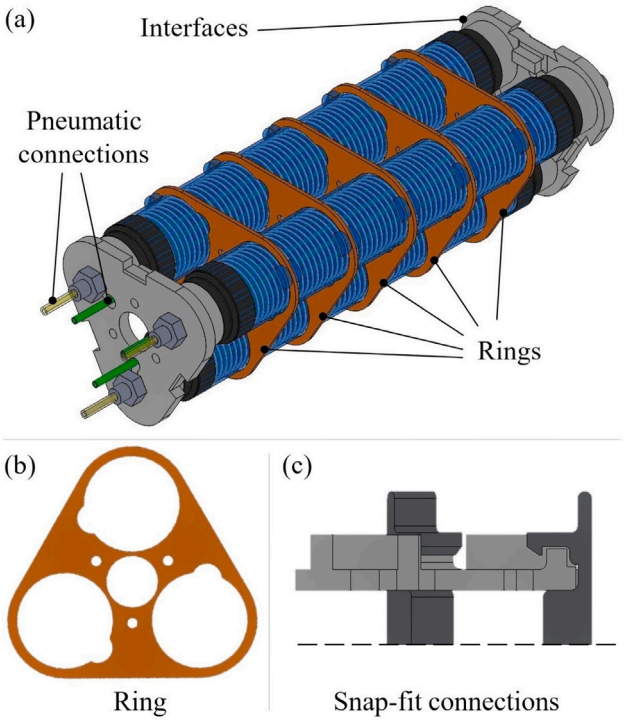

Fig. 2. (a) Design of the VARISA modules, (b) front view of the ring, and (c) cross-section view of the snap-fit connections of the interfaces, which are specular.

Five rings are arranged 20 mm apart along the module to keep the actuators in their correct working position (Fig. 2(b)). Indeed, without these rings, once inflated the actuators are free to buckle laterally and the bending capabilities are strongly reduced. Moreover, the ease of assembly of the interfaces was significantly improved through the use of snap—fit joints (Fig. 2(c)). Indeed, this approach preserves the lightness of the connection system in comparison with screws, while at the same time the ease of assembly and disassembly increases. The overall length of the arm is 285 mm, and its weight is 263 g.

2.3. Fabrication

The casting process of the outer chambers consists of injection moulding of silicone (Dragonskin 10, Smooth-On inc.). It is made using two 3D-printed resin hemi-shells and an inner core. In preliminary tests, we experienced how the friction between the single-piece inner core and cotton thread made it impractical to detach the outer chamber after casting without damaging it. We solved this issue by splitting the inner core into multiple parts so that the overall friction is also split and the disassembly can be managed without damaging the membrane. The developed inner core includes 6 interlocking 3D printed parts that are held in position through a 7.9 mm in diameter inner rod (Fig. 3). M3 and M4 holes are present on interlocking parts and the inner rod, respectively. The detailed fabrication steps of the outer membrane follow:

1. interlocking parts are assembled around the inner rod;
2. a layer of Parafilm is wounded around the core to avoid silicone leakages during casting (during this step is important to keep as constant as possible the thickness of the Parafilm layer to avoid asymmetries in the membrane thickness);

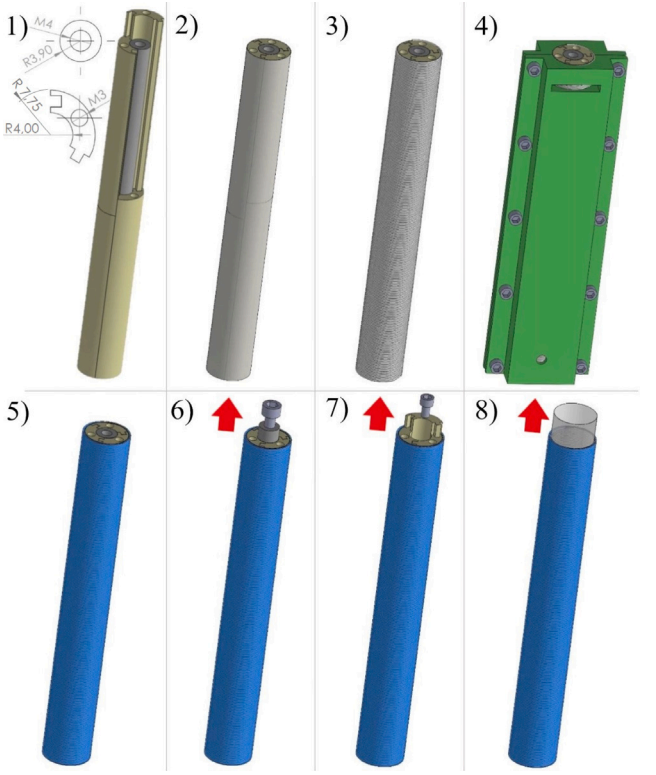

Fig. 3. Fabrication steps of the outer membranes and dimensions of the inner core (top left corner).

3. a cotton thread with 0.6 mm diameter is wounded around the inner core using additional strips of Parafilm to fix it to the extremities;
4. once the mould is closed with the inner core in position using nuts and bolts, uncured silicone is injected using a syringe through the hole on the bottom of the mould to fill the annular cavity;
5. after curing time the mould is opened leaving the outer chamber with the inner core;
6. a M4 bolt is inserted into the inner rod and used as an anchoring point to extract the rod;
7. similarly to the previous step, M3 bolts are used to extract the interlocking parts, which are free to slide axially;
8. the Parafilm layer is removed using tweezers.

The coupling between the cotton thread inner layer and the silicone outer layer ensures an integral axial deformation of the outer membrane when pressure is applied, making the typical IPAM behavior emerge. The hemi-shells are designed to include seats for the rings on the outer layer of the external membrane. The outer diameter and the thickness of the outer membrane are respectively 17.5 mm and 1 mm. The actuators can be then fabricated through the following steps (Fig. 4):

1. sheets of the end plates are obtained by cutting a 2 mm plexiglass sheet with a laser cutter;
2. fibers and guides are cut at 100 mm of length, while a single fiber which works as the pneumatic connection for the external chamber is cut at 500 mm of length;
3. the plates are bonded and the CT-joint is assembled by gluing fibers and guides in their housing seats;
4. the inner membrane is connected to the inner pneumatic connections to make the inner chamber;

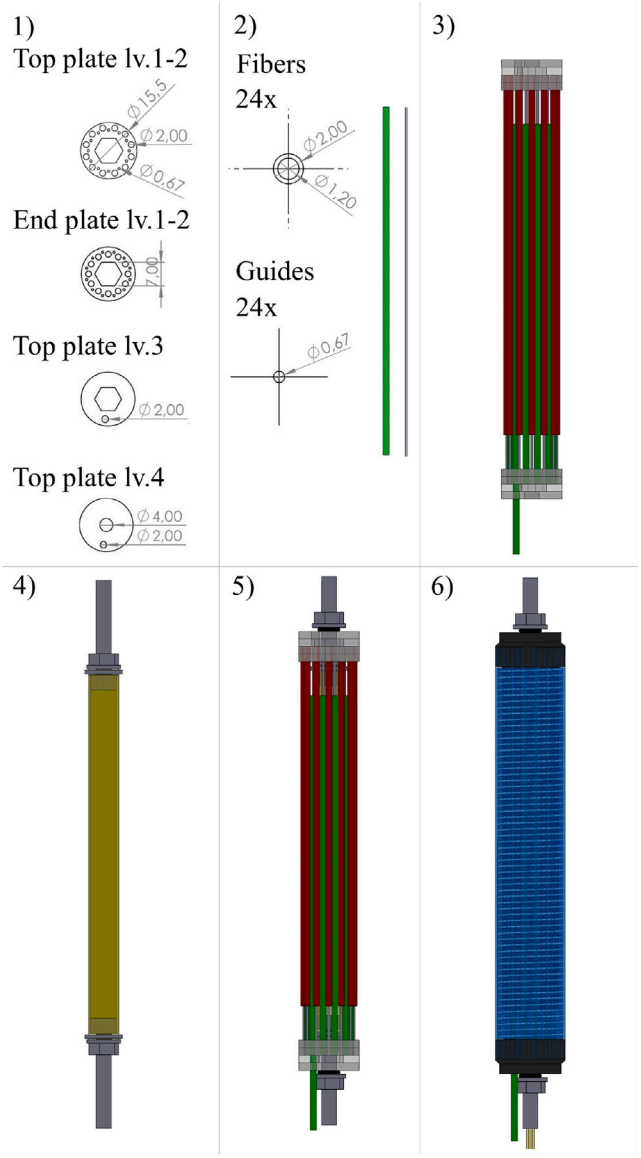

Fig. 4. Fabrication steps of the actuators and size of the plate discs (lv. 3 and 4 of the end plate only differ for the absence of the small hole).

5. the inner chamber is fixed to the end plates using washers and nuts (an o-ring is used between thread and nuts to ensure air tightness);
6. the CT-joint is inserted into the outer membrane, which is fixed to the end plates using insulating tape and a 2 mm Polypropylene (PP) tube is inserted into the drilled hole of the inner chamber to complete the pneumatic connections.

Regarding this last point, we experienced how once inflated the PP tube is slightly radially deformed. Inserting it into the drilled hole allows ensuring air tightness up to more than 4 bar because of friction without any additional gluing step. This of course makes the assembly/disassembly very quick.

The interfaces and the snap-fit connectors are 3D printed using a Rise 3D E2 printer and black PLA filament (Rise 3D Technologies, Inc.). Using 0.2 mm as layer height and 22% as infill percentage, the printing time for the two interfaces and the snap-fit connector is 2 h and 10 min. In order to withstand the stress induced by cyclic attachment and detachment of the interfaces, the snap-fit connectors need to be printed with a planar orientation. Indeed, any different orientation inevitably

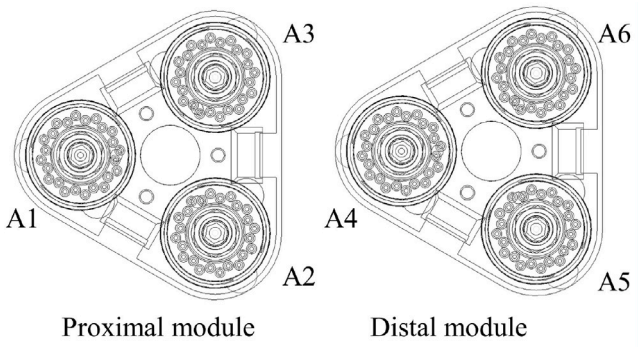

Fig. 5. Labels used to identify the actuators during the experimental tests.

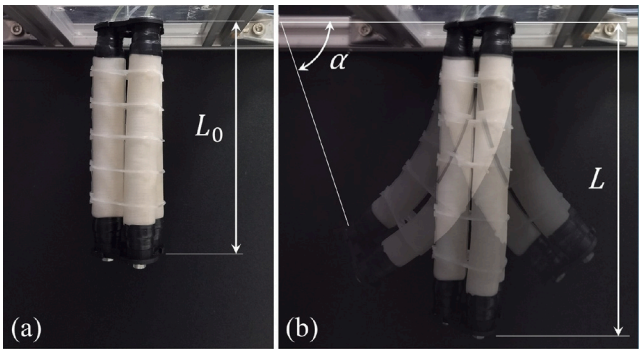

Fig. 6. (a) module in rest position and (b) during activation of A1:A3, A1, and A2-A3 (overlay); rest length, current length, and bending angle are also shown.

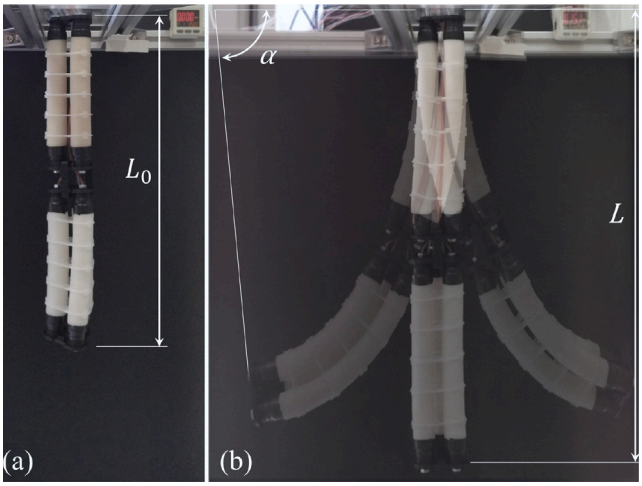

Fig. 7. (a) VARISA in rest position and (b) during activation of A1:A6, A1-A4 and A2-A3-A5-A6 (overlay); rest length, current length, and bending angle are also shown.

brings to mechanical failure through delamination. This is the reason why the snap-fit connectors are printed as separate parts rather than included in the interfaces. The rings are obtained by cutting a 1 mm PP sheet through a laser cutter. The seats for the chambers are designed with a notch that allows the actuators to easily slide along the rings during assembly and disassembly (Fig. 2(b)). Once the correct axial position is reached, the actuators are rotated by 90 deg to reach the proper orientation and preserve the relative position between actuators and rings.

Once all components are fabricated, the rings and the actuators are coupled and then the interfaces are fixed to the end caps of the actuators using nuts. This completes the fabrication of the module. The proximal and the distal modules are connected using the snap-fit connectors and passing the six pneumatic tubes of the distal module through the central hole of the proximal module. Finally, the latter is fixed to the frame using M3 nuts and bolts.

2.4. Characterization protocol

In this section, the procedures of the experimental tests are reported. Each test was repeated three times and both mean values and standard deviations were calculated. Both the single module and the arm were characterized following the same protocol to assess both the deformation and the stiffness variation capabilities in quasi-static conditions. For convenience, the tests are here reported in order of aim, while in Section 3 the performances are reported and discussed starting from the module and then moving to the arm. The labels adopted to indicate the active actuators during the tests on the arm are reported in Fig. 5. Labels A1:A3 are also used for the tests on the single module. A compressor (Leonardo 101, FIAC Air Compressors S.p.A.) was used together with twelve 3/2 valves (VDW200/300, SMC Corp.) (inner and outer chambers of each actuator) to set the air pressure inputs controlled via two Arduino Due boards.

2.4.1. Deformation tests

Pressure-strain tests were performed to evaluate the deformation capabilities of both the single module (Fig. 6) and the whole arm (Fig. 7). Tests were executed in the pressure range 0–150 kPa with steps of 10 kPa. A digital camera was used to capture the deformations and thereafter the software Tracker was used to extract the measurements.

The pressure-elongation test of the single module (test D1) was executed activating both the inner and the outer chamber of A1:A3. The elongation ΔL was evaluated as the difference between current length L and rest length L_0 (Fig. 6).

The pressure-bending tests of the single module (test D2) were performed in each bending plane with activation of A1, A2, and A3 for the counterclockwise direction and A2-A3, A1-A3, and A1-A2 for the clockwise direction. The bending angle α was measured as shown in Fig. 6(b).

The pressure-elongation test of the whole arm (test D3) was executed activating both the inner and the outer chamber of A1:A6. The elongation ΔL was evaluated as in test D1 (Fig. 7).

Similarly to test D2, the pressure-bending tests of the whole arm (test D4) were carried out in each bending plane with activation of A1-A4, A2-A5, and A3-A6 for the counterclockwise direction and A2-A3-A5-A6, A1-A3-A4-A6, and A1-A2-A4-A5 for the clockwise direction. The bending angle α was measured as shown in Fig. 7(b).

2.4.2. Stiffness variation tests

To evaluate the stiffness variation capabilities of both the single module (Fig. 8) and the whole arm (Fig. 9) additional components were included in the testing setup. In particular, a linear bearing was used to horizontally displace the free end of both the single module and the whole arm in different activation configurations, and concurrently, evaluate the force through a load cell (Mini45, ATI Industrial Automation). A servomotor (Hitech HS 785-HB) was used to move the slide back and forth at a velocity of 140 mm/min. An indenter made of plexiglass was connected to the load cell to exert forces on the bottom interface of the modules.

After simultaneous pressurization of both the inner and the outer chambers of the actuators and once reached the desired module deformation, the outer chambers were opened to atmospheric pressure. Then, the pressure of the inner chamber of all chambers, both active and inactive ones during deformations, was adjusted to achieve the desired differential pressure (dP). In particular in each test, dP equal to 0, 50, 100, 150 and 200 kPa were reached. In preliminary tests, the

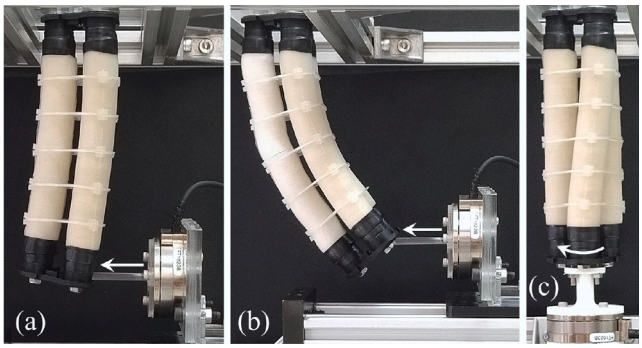

Fig. 8. Stiffness tests of the single module: bending stiffness at (a) rest length and (b) 45 deg bending, and (c) torsional stiffness test at rest length.

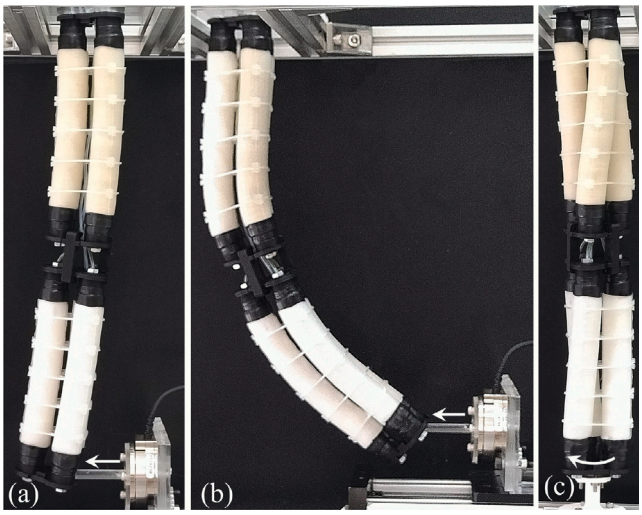

Fig. 9. Stiffness tests of the whole arm: bending stiffness at (a) rest length and (b) 45 deg bending, and (c) torsional stiffness test at rest length.

response of the module in different load directions was compared and no significant differences emerged. Therefore, a similar protocol was adopted in the subsequent tests.

The bending stiffness of the single module was evaluated in the range of displacement 0–15 mm with the load cell set to acquire the force values with a 2.5 mm step. Tests were first executed with activation of A1:A3 at rest length (Fig. 8(a)), at 25%, and at 50% of strain of the actuators (test S1), hereafter called simply strain. Then, the module was bent to reach a 45-degree bending angle with activation of A1, A2, and A3 (test S2) repositioning the load cell as shown in Fig. 8(b). Next, the torsional stiffness of the single module was evaluated. The top of the load cell was connected through a PLA interface to the bottom of the single module, while a second PLA interface was used to connect the lower face directly to the servomotor (Fig. 8(c)). A 22.5 degree clockwise torsion angle was applied setting the load cell to acquire the torque values with a 3.75 degree step. The test was executed at both rest length and 50% of strain (Test S3).

Subsequently, tests were performed to assess the bending stiffness of the whole arm. The range of displacement was doubled to 0–30 mm always with a 2.5 mm step for sampling. Similarly to test S1, the bending stiffness was first assessed at rest length (Fig. 9(a)), 25%, and 50% of strain with activation of A1:A6 (test S4). Next, the arm was bent to reach a 45-degree bending angle with activation of A1, A2, and A3 (test S5) as shown in Fig. 9(b). Then, tests on the torsional stiffness of the arm were performed with the same configuration of the load cell reported for test S3 (Fig. 9(c)). The torsion angle was doubled to 45 deg and the torque values were acquired with a 3.75 degree step. The test was executed at both rest length and 50% of strain (Test S6).

3. Results and discussion

In this section the results of the tests are reported, first regarding the single module and then on the whole VARISA. For all tests, the graphs report mean values as solid lines, while the standard deviations are reported as shaded areas of the same color.

3.1. Single module

Results of test D1 are reported in Fig. 10(a). The elongation of the module linearly increases up to 100 kPa. Then, the slope of the curve gradually decreases up to 48 mm at 150 kPa, which represents almost 50% of strain and a 38.4% increase in the length of the module. Although a further elongation would be possible with an additional increase of the input pressure, the value of 150 kPa represents a reasonable safety limit. Indeed, with higher elongations, the risk of undesired deformations (e.g. mechanical instabilities of the fibers, delamination of the outer membranes) increases. In the tested range, the fibers never experienced buckling and the original configuration was always fully restored. A similar behavior emerges from the results of test D2, which are reported in Fig. 10(b). In particular, for counterclockwise and clockwise directions, the bending angle linearly increases up to respectively 110 kPa and 125 kPa. In both cases, fluctuations are present in the range of 50–100 kPa, while the overall trend is maintained. Then, a plateau is reached at 45 and 50 degrees for respectively counterclockwise and clockwise directions. From an analytical point of view, the two bending angles should be equal. Indeed, this value can be assumed as proportional to the pressure moment and inversely proportional to the bending stiffness of the structure. Thanks to the disposition at 120 degrees, the pressure moment of a single actuator M_1 is equal to the one given by two actuators: $2 \times M_1 \times cos(60deg) = 2 \times 0.5 \times M_1$. The difference between the two cases actually emerges from the experimental tests in light of the different number of inactive actuators, which act antagonistically and dissipate energy to be bent and also stretched, resulting in a variation on the neutral axis of bending position (see supplementary material). The presence of the threshold in bending instead, is partially addressable considering that the CT-Joint, even at dP = 0 kPa, possesses a non negligible bending stiffness. Remarkably, also at the end of this test, the coupling between fibers and guides is completely preserved. This behavior emerges from the interaction of all components of the actuators. Therefore, it is a consequence of both the design and the material selection of CT-joint and membranes. Moreover, this result is difficult to be reached with different approaches reported in the literature and makes the use of Fiber Jamming and the CT-Joint architecture a viable solution when variable stiffness devices need to be coupled with systems capable of large and multi-directional deformations.

Both in tests D1 and D2 the standard deviations are very low, compared to the mean values. Therefore, the repeatability of the different actuators is also verified. This aspect underlines how the fabrication process is robust against the variability which usually emerges from manual fabrication and assembly steps.

The results reported in Fig. 11 highlight how it is possible to significantly tune the stiffness of the module at different elongations (test S1). In all cases, an initial pre-slip state is visible, followed by a subsequent post-slip state, as expected on systems based on jamming transition. The first state is characterized by a linear relation between force and displacement, while the force gradually decreases with slopes proportional to dP in the second state. As reported in our previous work on the VSLA [31], this aspect emerges from the dynamic friction that CT-joint components develop during sliding. Moreover, no significant differences emerge in the residual deformations, which are in the range 30%–50% of the applied displacement. These non-negligible

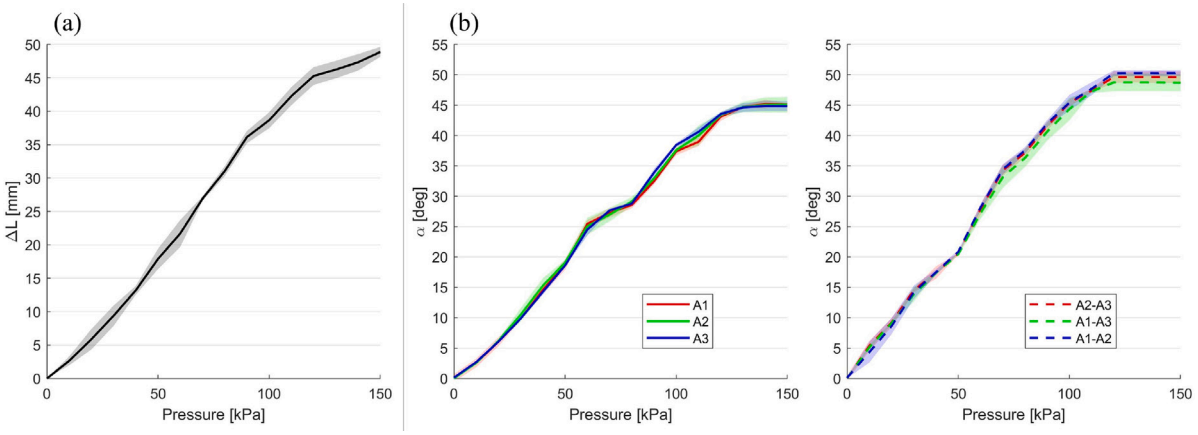

Fig. 10. Results of tests (a) D1 (elongation of the module VS pressure input) and (b) D2 (bending of the module VS pressure input) for counterclockwise and clockwise directions.

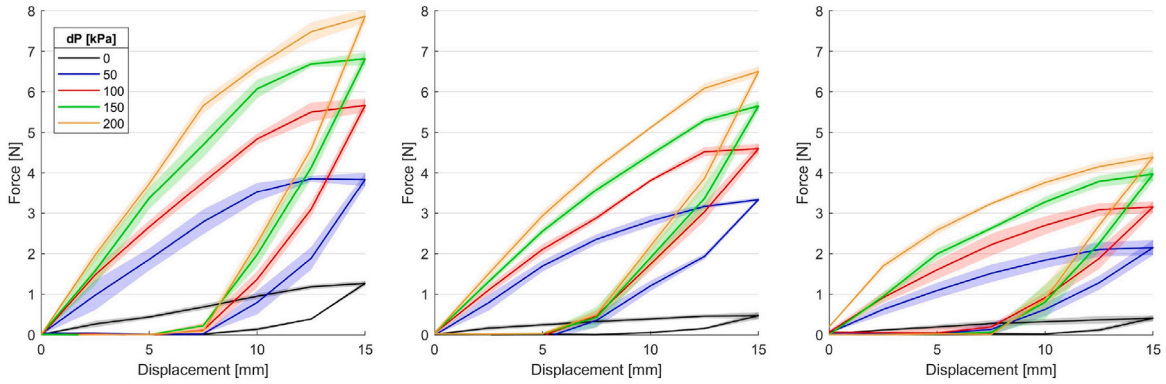

Fig. 11. Results of test S1 (bending stiffness of the module VS differential pressure and displacement) at rest length, 25%, and 50% of strain, from left to right.

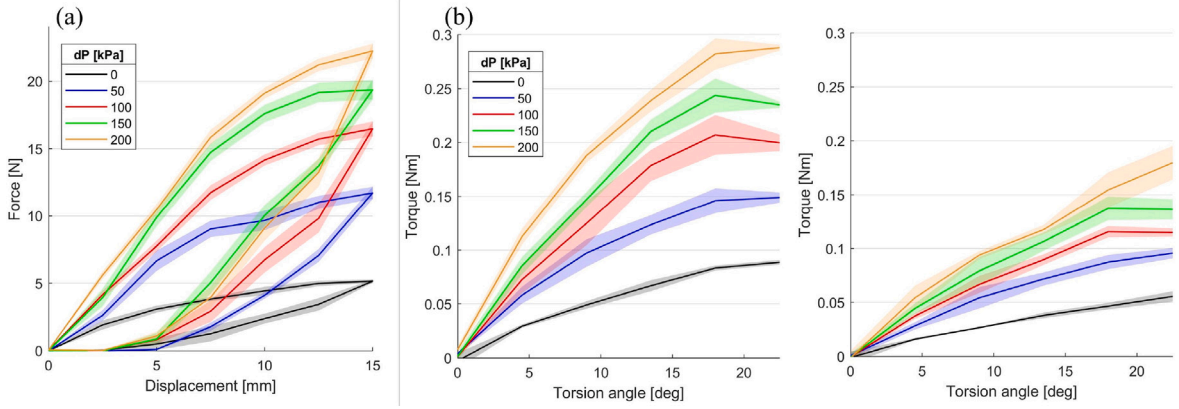

Fig. 12. Results of tests (a) S2 (Bending stiffness of the module in bent configuration VS differential pressure and displacement) and (b) S3 (torsional stiffness of the module VS differential pressure and rotation) at rest length and 50% of strain, from left to right.

values make the modules suitable also for applications where energy dissipation is required, like for impact absorption.

To better capture the results of all stiffness tests, two metrics have been used: the ratio of bending stiffnesses at 15% of the overall displacement $R_{k,b} = K_{b,on}/K_{b,off}$ and the ratio of forces at maximum displacement $R_f = F_{on}/F_{off}$. These allow evaluating the behavior of the module in pre-slip state and in the entire tested range, respectively. The results of tests on the module are reported in Table 1. Regarding test S1 both $R_{k,b}$ and R_f tend to increase with dP and from 0 to 50% strain. This behavior, which is peculiar of the VSLA, also emerges from the module since the actuators work in parallel. It derives from the architecture of the CT-Joint, which preserves its VS contribution during elongation. Moreover, in absolute terms, both the stiffness and the maximum force gradually decrease with the strain, with reductions of respectively 15% and 40% in the tested range.

From the comparison between the values of force of test S2 (Fig. 12(a)) and S1 (Fig. 11), a significant rise of the load-bearing capabilities emerges when the module is subject to both transversal and axial loads. Indeed, in this case, the pre-slip state is preserved up to 50% of the applied displacement. Moreover, the stiffness in this region ranges from 0.76 to 3.14 N/mm and 23N are required to deflect the module with dP = 200 kPa. The ratios are instead lower, as reported in Table 1. In this case, the residual deformations are in the range 15%–30% of the applied displacement and indicate a reduction of the plastic

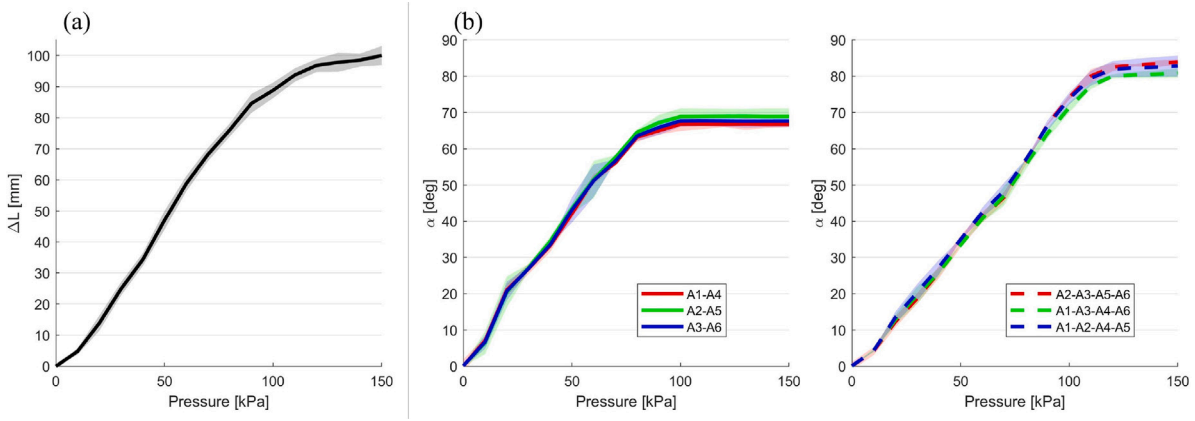

Fig. 13. Results of tests (a) D3 (elongation of the arm VS pressure input) and (b) D4 (bending of the arm VS pressure input) for counterclockwise and clockwise directions.

Table 1
Values of $R_{k,b}$, $R_{k,t}$, R_f, and $R_{k,t}$ for tests S1, S2, and S3.

Test	Strain [%]	dP [kPa]	$R_{k,b}$	R_f
S1	0	50	3.69 ± 1.36	3.03 ± 0.35
		100	5.41 ± 0.78	4.47 ± 0.68
		150	5.59 ± 1.23	4.89 ± 0.93
		200	6.77 ± 1.06	5.64 ± 1.37
	25	50	4.15 ± 0.87	3.88 ± 0.32
		100	5.79 ± 0.65	5.35 ± 0.79
		150	6.88 ± 0.58	6.57 ± 0.82
		200	7.03 ± 0.96	7.64 ± 1.04
	50	50	5.41 ± 1.58	5.28 ± 1.88
		100	7.15 ± 1.56	8.20 ± 1.97
		150	7.81 ± 1.30	9.31 ± 1.33
		200	10,41 ± 0.90	10.54 ± 1.20
S2	/	50	1.08 ± 0.62	2.12 ± 0.67
		100	2.33 ± 0.70	3.35 ± 0.82
		150	2.93 ± 1.05	4.03 ± 1.12
		200	4.11 ± 1.02	4.45 ± 0.98
			$R_{k,t}$	R_t
S3	0	50	2.24 ± 0.85	1.90 ± 0.71
		100	2.90 ± 0.98	2.46 ± 0.89
		150	3.22 ± 0.55	2.84 ± 0.20
		200	3.41 ± 0.49	3.27 ± 0.45
	50	50	2.18 ± 0.60	2.21 ± 0.88
		100	2.73 ± 0.45	2.66 ± 0.64
		150	2.20 ± 0.85	2.93 ± 1.10
		200	3.55 ± 0.92	3.27 ± 1.55

behavior in comparison with test S1, while the energy dissipation is preserved.

The results of test S3 (Fig. 12(b)) underlined that the torsional stiffness can also be varied by increasing dP. In Table 1, $R_{k,t}$ and R_t are used to indicate the ratio of torsional stiffnesses at 20% of the applied rotation and at maximum torque. In particular, at rest length and 200 kPa, 2.9 N applied at a distance of 100 mm are required to rotate the module of 22.5 degrees, while the same value is reduced of 38% at 50% strain. However, the torsional and the bending stiffness variation are not comparable. This reflects the design of the CT-joint, which is optimized for axial and bending loads.

3.2. Arm

The results of test D3 are reported in Fig. 13(a). The elongation of the two coupled modules linearly increases with the pressure up to 85 mm at 90 kPa. Then, the slope of the elongation curve decreases gradually up to 101 mm at 150 kPa, which is 50% of the strain and 35.4% of the whole arm length. This value is also slightly higher than twice the maximum elongation of the single module. This result reflects the higher elongation of the proximal module, which is not only subject to the provided pressure but also to the weight of the distal module. The standard deviation is very small for low pressures and remains contained for the higher ones.

The effect of the weight of the distal module on the proximal one also emerges from the results of test D4 (Fig. 13(b)). In particular, the bending angle of the proximal module is limited in both testing conditions. The overall bending linearly increases up to 85 kPa and 110 kPa for counterclockwise and clockwise directions, respectively. For higher pressures, it rapidly reaches the plateau values of respectively 69.5 and 82 degrees. As for the single module, no significant difference is visible in the VARISA behavior in the three bending planes. To better visualize the displacement behavior of the arm, the position of the tip in the space during tests D3 and D4 is reported in Fig. 14. The path of the end tip during bending results quite flattened up to high pressure inputs, where the subsequent positions are clustered and slightly diverge from the initial plane. The almost planar rather than hemispherical workspace is a consequence of the stretch of the inactive actuators, which is also the reason behind the plateau in test D4. In any case, in elongation the arm can reach points that are 100 mm below its rest condition and span an almost planar circular space with a diameter of 300 mm. The speed of the arm to reach the desired deformed condition was also evaluated. On average, the VARISA takes 0.7 s to reach the final deformed state, and 1.6 s to return in rest position. These results suggest how the friction in between the CT-Joints is overcome by the elastic rebound force of the silicone chambers in the VSLAs in a relatively fast transition time.

Regarding the stiffness variation, results of test S4 (Fig. 15) show that applying twice the displacement used in test S1 the resulting forces are sensibly lower. However, the qualitative behavior is similar, with a pre-slip and a post-slip region, and more importantly, it still allows to significantly tune the stiffness at different elongations. The ratios of stiffnesses and forces are reported in Table 2. For S4 (as for S1) both $R_{k,b}$ and R_f gradually increase with dP and from 0 to 50% strain. Interestingly, this peculiar behavior emerges also for the arm, in which the actuators work both in series and parallel. Regarding the absolute measurements, the difference in the applied displacement does not allow to directly compare S4 with S1. However, as for the single module, also for the whole VARISA the value of both stiffness and the maximum force tends to decrease with the strain, with reductions of respectively 24% and 44% in the tested range. The residual deformations are instead greater than in S1, being in the range 40%–60% of the applied displacement. This result is in line with the fact that the actuators of the two modules work in series.

Similarly to test S2, the load-bearing capability of the arm significantly increases in test S5 (Fig. 16(a)). In particular, the stiffness goes from 0.06 to 0.52 N/mm increasing dP, and at 200 kPa it is necessary to apply 9.82 N to deflect the end tip of the arm of 30 mm, which

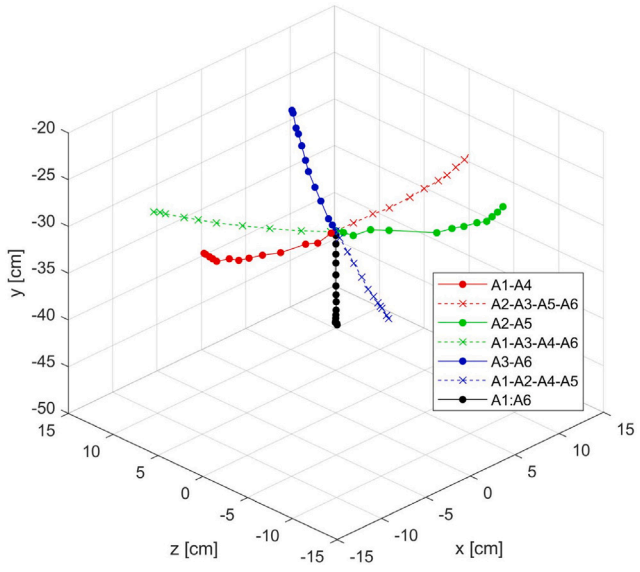

Fig. 14. Position of the tip of the VARISA in the 3D space for the different activation patterns.

Table 2
Values of $R_{k,b}$, $R_{k,t}$, R_f, and $R_{k,t}$ for tests S4, S5, and S6.

Test	Strain [%]	dP [kPa]	$R_{k,b}$	R_f
S4	0	50	5.90 ± 0.96	3.35 ± 0.78
		100	6.60 ± 0.72	4.68 ± 0.32
		150	7.05 ± 1.03	5.49 ± 0.43
		200	8.12 ± 1.16	6.63 ± 0.87
	25	50	6.17 ± 0.37	4.60 ± 0.43
		100	6.59 ± 0.55	6.34 ± 0.89
		150	7.67 ± 0.58	7.66 ± 1.06
		200	9.48 ± 0.66	8.52 ± 0.94
	50	50	5.03 ± 1.08	2.51 ± 0.86
		100	6.35 ± 0.56	3.42 ± 0.92
		150	7.26 ± 0.80	4.41 ± 0.84
		200	9.57 ± 1.27	4.97 ± 1.28
S5	/	50	3.18 ± 1.51	1.92 ± 0.46
		100	6.08 ± 1.42	3,48 ± 0.77
		150	7.43 ± 1.87	4.46 ± 0.90
		200	8.69 ± 1.22	4.97 ± 1.15
			$R_{k,t}$	R_t
S6	0	50	1.87 ± 0.36	1.73 ± 0.60
		100	2.02 ± 0.28	2.19 ± 0.92
		150	2.45 ± 0.45	2.48 ± 0.97
		200	3.19 ± 0.51	2.93 ± 1.03
	50	50	1.23 ± 0.20	1.74 ± 0.10
		100	1.61 ± 0.26	2.30 ± 0.78
		150	2.38 ± 0.41	2.76 ± 1.05
		200	3.40 ± 0.44	3.08 ± 1.22

is approximately 10% of the VARISA length. However, unlike test S1-S2, the VS capability is better preserved in S5 in comparison with S4, as reported in Table 2. This result once again reflects the modular architecture of the arm with actuators disposed in series. Moreover, as the single module, the whole arm shows lower residual deformations in bending.

Lastly, the results of test S6 are reported in Fig. 16(b). As for test S3 in Table 2, $R_{k,t}$ and R_t are used to indicate the ratio of torsional stiffnesses at 20% of the applied rotation and at maximum torque. When the arm is at rest length and dP = 200 kPa, the application of 2.6 N at a distance of 100 mm causes a module rotation of 45 degrees, while the same rotation is reached with a force value reduced of 45% at 50% strain.

Table 3
Comparison of the VARISA with other VS soft arms of similar scale. FJ: Fiber Jamming, CMJ: Chain Mail Jamming, AA: Antagonistic Actuation.

	Stiffening principle	R	Workspace [cm^3]
Xie et al. [27]	CMJ	3.74	12 × 12 × 12
Le et al. [16]	Thermal	5.00	4.5 × 4.5 × 4.5
Giannaccini et al. [12]	AA	4.11	9 × 30 × 30
VARISA	FJ	9.57	10 × 30 × 30

4. Conclusions

In this work, we introduced the VARISA based on pneumatic actuation and fiber jamming. We adopted a modular architecture with two equal modules connected in series, and three actuators for each module to enable both elongation and multidirectional bending. The module design is built upon the first version of the recently introduced VSLA. The actuators were designed to target both large deformability and significant VS. In particular, the designed caps guarantee air tightness, a proper connection of the actuators to the interfaces, and fast and easy assembly steps. Moreover, the tailored fabrication process developed for the outer membrane allowed partial embedding of an inextensible cotton thread in a single silicone layer. Membranes fabricated through this process possess a very reduced thickness without scarifying the proper functionality and reliability of the IPAM.

From the results of the experimental tests it is evident how the presence of components required for the VS only partially affects the deformability and the workspace dimensions of the arm. At a maximum input pressure of 150 kPa, it is indeed capable of 100 mm elongation, 82 degree bending, and to cover a 300 mm lateral distance in bending. Remarkably, during the execution of these tests, the coupling between fibers and guides was always preserved and no buckling of fibers occurred. This last qualitative result suggests that our choices for the inner and outer membrane, together with the CT-joint configuration make the fiber jamming technology able to stably operate for repetitive cycles of activation.

When the differential pressure between inner and outer chamber rises up, the bending stiffness of the arm rapidly increases of almost an order of magnitude (stiffness ratio at dP = 200 kPa between 8.12 and 9.57) in all tested conditions. The load-bearing capabilities also increase significantly with dP: the force required to deflect of 10% of the VARISA length its tip ranges from 0.42 N to 2.8 N at rest condition, and from 1.9 to 9.81 N in bent configuration. The torsional stiffness instead rises up almost three times, but with lower load bearing capability. In terms of VS, the achieved results are superior to what is reported for soft robotics platforms based on granular jamming. However, the VS performances are lower than the ones reported for layer jamming based structures. Nevertheless, we wish to empathize how these better literature results were reached on endoscopes, hence devices with size and workspace significantly lower. Thus, the potential of the presented approach is more evident through a concurrent evaluation of both VS capabilities and the relatively large workspace. Moreover, the presented approach potential emerges from Table 3, in which both R (measured with the same algorithm reported in Section 1) and the workspace of the VARISA are reported together with the ones of soft arms with a comparable workspace.

The proposed approach was completely technological driven. In future works, we aim to scale up the size of the arm evaluating the variability over different ranges and its implications on the dynamic response. This will easy the exploitation of the proposed approach in more specific applications. The VARISA is indeed potentially suitable for applications where energy dissipation is required, like for impact absorption or in human-machine interaction. In these scenarios, collaborative robots (Cobots) are nowadays used for their ability to work next to human workers. However, due to the safety standards, the operating

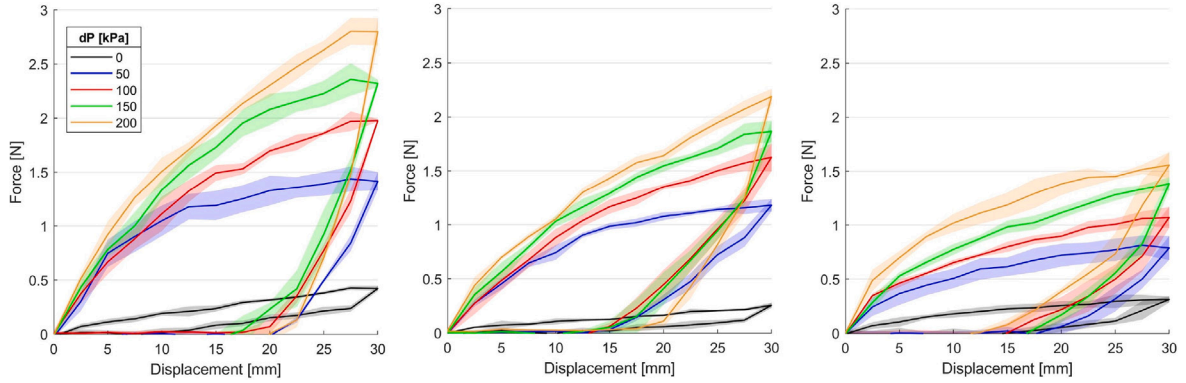

Fig. 15. Results of test S4 (bending stiffness of the VARISA VS differential pressure and displacement) at rest length, 25%, and 50% of strain, from left to right.

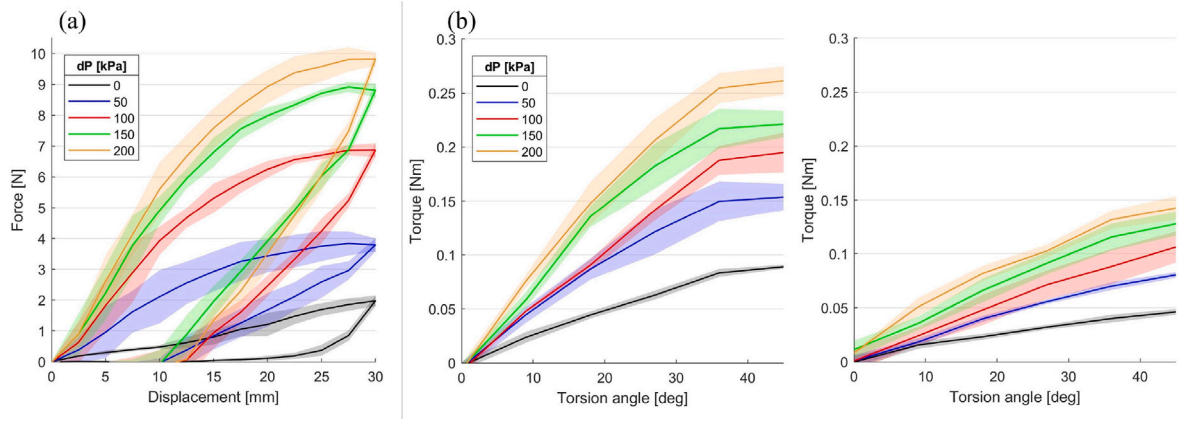

Fig. 16. Results of tests (a) S5 (Bending stiffness of the VARISA in bent configuration VS differential pressure and displacement) and (b) S6 (torsional stiffness of the arm VS differential pressure and rotation) at rest length and 50% of strain, from left to right.

speed of the Cobot must be significantly reduced when a worker is in the workspace [33]. This limitation comes from the need to reduce the amount of kinetic energy and therefore the risk of injuries in case of an impact. This quantity is high also in light of the rigid structure of which Cobots are made. On one hand, the proposed arm adoption is limited to the execution of tasks with limited payloads (e.g. in supporting an operator during the manual assembly steps of light devices). On the other one, in the soft state the arm is safe without the need to reduce the operating speed, while at target position reached, the stiff state can be activated to withstand the applied forces.

This research did not receive any specific grant from funding agencies in the public, commercial, or not-for-profit sectors.

CRediT authorship contribution statement

Luca Arleo: Conceptualization, Data curation, Formal analysis, Investigation, Methodology, Project administration, Software, Validation, Visualization, Writing – original draft, Writing – review & editing. **Matteo Cianchetti:** Data curation, Formal analysis, Methodology, Project administration, Supervision, Writing – review & editing.

Declaration of competing interest

The authors declare that they have no known competing financial interests or personal relationships that could have appeared to influence the work reported in this paper.

Data availability

No data was used for the research described in the article.

Appendix A. Supplementary data

Supplementary material related to this article can be found online at https://doi.org/10.1016/j.mechatronics.2024.103230.

References

[1] Hawkes EW, Majidi C, Tolley MT. Hard questions for soft robotics. Science Robotics 2021;6.

[2] Manti M, Cacucciolo V, Cianchetti M. Stiffening in soft robotics: A review of the state of the art. IEEE Robot Autom Mag 2016;23(3):93–106. http://dx.doi.org/10.1109/MRA.2016.2582718.

[3] Wolf S, Hirzinger G. A new variable stiffness design: Matching requirements of the next robot generation. In: 2008 IEEE international conference on robotics and automation. 2008, p. 1741–6. http://dx.doi.org/10.1109/ROBOT.2008.4543452.

[4] Catalano MG, Grioli G, Garabini M, Bonomo F, Mancini M, Tsagarakis N, Bicchi A. VSA-CubeBot: A modular variable stiffness platform for multiple degrees of freedom robots. In: 2011 IEEE international conference on robotics and automation. 2011, p. 5090–5. http://dx.doi.org/10.1109/ICRA.2011.5980457.

[5] Kim B-S, Song J-B. Design and control of a variable stiffness actuator based on adjustable moment arm. IEEE Trans Robot 2012;28(5):1145–51. http://dx.doi.org/10.1109/TRO.2012.2199649.

[6] Deng L, Sun S, Christie MD, Li W, Ning D, Du H, Zhang S, Li W. Innovative variable stiffness and variable damping magnetorheological actuation system for robotic arm positioning. J Intell Mater Syst Struct 2023;34(2):123–37. http://dx.doi.org/10.1177/1045389X221099453.

[7] She Y, Gu Z, Song S, Su H-J, Wang J. Design, modeling, and manufacturing of a variable lateral stiffness arm via shape morphing mechanisms. J Mech Robot 2021;13(3). http://dx.doi.org/10.1115/1.4050379.

[8] Stilli A, Grattarola L, Feldmann H, Wurdemann HA, Althoefer K. Variable stiffness link (VSL): Toward inherently safe robotic manipulators. In: 2017 IEEE international conference on robotics and automation. 2017, p. 4971–6. http://dx.doi.org/10.1109/ICRA.2017.7989578.

[9] Fu J, Lin H, Xu W, Gan D. A novel variable stiffness compliant robotic link based on discrete variable stiffness units for safe human-robot interaction. In: 46th Mechanisms and robotics conference, vol. 7. 2022, http://dx.doi.org/10.1115/DETC2022-89825.
[10] Manti M, Pratesi A, Falotico E, Cianchetti M, Laschi C. Soft assistive robot for personal care of elderly people. In: 2016 6th IEEE international conference on biomedical robotics and biomechatronics. 2016, p. 833–8. http://dx.doi.org/10.1109/BIOROB.2016.7523731.
[11] Sui D, Zhao S, Wang To. Design of a bio-inspired extensible continuum manipulator with variable stiffness. J Bionic Eng 2022. http://dx.doi.org/10.1007/s42235-022-00213-0.
[12] Giannaccini ME, Xiang C, Atyabi A, Theodoridis T, Nefti-Meziani S, Davis S. Novel design of a soft lightweight pneumatic continuum robot arm with decoupled variable stiffness and positioning. Soft Robot 2018;5(1):54–70. http://dx.doi.org/10.1089/soro.2016.0066.
[13] Ma N, et al. Bioinspir Biomim 2024;19.
[14] Chen S, Pang Y, Cao Y, Tan X, Cao C. Soft robotic manipulation system capable of stiffness variation and dexterous operation for safe human–machine interactions. Adv Mater Technol 2021;6(5):2100084. http://dx.doi.org/10.1002/admt.202100084.
[15] Pagliarani N, Arleo L, Albini S, Cianchetti M. Variable stiffness technologies for soft robotics: A comparative approach for the STIFF-FLOP manipulator. Actuators 2023;12(3). http://dx.doi.org/10.3390/act12030096.
[16] Le HM, Cao L, Do TN, Phee SJ. Design and modelling of a variable stiffness manipulator for surgical robots. Mechatronics 2018;53:109–23. http://dx.doi.org/10.1016/j.mechatronics.2018.05.012.
[17] Le H, Phan P, Lin Co. A temperature-dependent, variable-stiffness endoscopic robotic manipulator with active heating and cooling. Ann Biomed Eng 2020;48:1837–49. http://dx.doi.org/10.1007/s10439-020-02495-z.
[18] Zhang M, Chen X, Sun Y, Gan M, Liu M, Tang S-Y, Zhang S, Li X, Li W, Sun L. A magnetically and thermally controlled liquid metal variable stiffness material. Adv Energy Mater 2023;25(6):2201296. http://dx.doi.org/10.1002/adem.202201296.
[19] Zhou X, Shu J, Jin H, Ren H, Ma G, Gong N, et al. Variable stiffness wires based on magnetorheological liquid metals. Int J Smart Nano Mater 2022;13(2):232–43. http://dx.doi.org/10.1080/19475411.2022.2065703.
[20] Falco ID, Cianchetti M, Menciassi A. A soft multi-module manipulator with variable stiffness for minimally invasive surgery. Bioinspiration Biomim 2017;12(5):056008. http://dx.doi.org/10.1088/1748-3190/aa7ccd.
[21] Ranzani T, Cianchetti M, Gerboni G, Falco ID, Menciassi A. A soft modular manipulator for minimally invasive surgery: Design and characterization of a single module. IEEE Trans Robot 2016;32(1):187–200. http://dx.doi.org/10.1109/TRO.2015.2507160.
[22] Yamane S, Wakimoto S. Development of a flexible manipulator with changing stiffness by granular jamming. In: 2017 24th International conference on mechatronics and machine vision in practice. 2017, p. 1–5. http://dx.doi.org/10.1109/M2VIP.2017.8211491.
[23] Xu F-Y, Jiang F-Y, Jiang Q-S, Lu Y-X. Soft actuator model for a soft robot with variable stiffness by coupling pneumatic structure and jamming mechanism. IEEE Access 2020;8:26356–71. http://dx.doi.org/10.1109/ACCESS.2020.2968928.
[24] Yang Y, Qi Y, Pan P, Zhao Y, Zhong S, Yang Y. Oscillation suppression in a particle robotic arm by stiffness and damping regulation. Mechatronics 2022;85:102819. http://dx.doi.org/10.1016/j.mechatronics.2022.102819.
[25] Jiang A, Xynogalas G, Dasgupta P, Althoefer K, Nanayakkara T. Design of a variable stiffness flexible manipulator with composite granular jamming and membrane coupling. In: 2012 IEEE/RSJ international conference on intelligent robots and systems. 2012, p. 2922–7. http://dx.doi.org/10.1109/IROS.2012.6385696.
[26] Zhao Y, et al. Bioinspir Biomim 2019;14.
[27] Xie Z, Mohanakrishnan M, Wang P, Liu J, Xin W, Tang Z, et al. Soft robotic arm with extensible stiffening layer. IEEE Robot Autom Lett 2023;1–7. http://dx.doi.org/10.1109/LRA.2023.3268012.
[28] Kim Y-J, Cheng S, Kim S, Iagnemma K. A novel layer jamming mechanism with tunable stiffness capability for minimally invasive surgery. IEEE Trans Robot 2013;29(4):1031–42. http://dx.doi.org/10.1109/TRO.2013.2256313.
[29] Amanov E, Nguyen T, Markmann So. Toward a flexible variable stiffness endoport for single-site partial nephrectomy. Ann Biomed Eng 2018;46:1498–510. http://dx.doi.org/10.1007/s10439-018-2060-4.
[30] Shah DS, Yang EJ, Yuen MC, Huang EC, Kramer-Bottiglio R. Jamming skins that control system rigidity from the surface. Adv Funct Mater 2021;31(1):2006915. http://dx.doi.org/10.1002/adfm.202006915.
[31] Arleo L, Lorenzon L, Cianchetti M. Variable stiffness linear actuator based on differential drive fiber jamming. IEEE Trans Robot 2023;1–14. http://dx.doi.org/10.1109/TRO.2023.3236941.
[32] Arleo L, Stano G, Percoco G, Cianchetti M. I-support soft arm for assistance tasks: a new manufacturing approach based on 3D printing and characterization. Prog Addit Manuf 2021;6:243–56. http://dx.doi.org/10.1007/s40964-020-00158-y.
[33] Aaltonen I, Salmi T. Experiences and expectations of collaborative robots in industry and academia: barriers and development needs. Procedia Manuf 2019;38:1151–8. http://dx.doi.org/10.1016/j.promfg.2020.01.204, 29th International Conference on Flexible Automation and Intelligent Manufacturing (FAIM 2019), June 24-28, 2019.

Luca Arleo received the Ph.D. in Biorobotics from Sant'Anna School of Advanced Studies, Pisa, Italy, in 2024. He is currently member of the Soft Mechatronics for Biorobotics Lab, BioRobotics Institute, Scuola Superiore Sant'Anna, Pontedera, Pisa, Italy. His research interests include soft robotics, soft actuators, additive manufacturing, variable stiffness, and bioinspired design.

Matteo Cianchetti received the Ph.D. degree in biorobotics from Scuola Superiore Sant'Anna, Pisa, Italy, in 2011. He is currently an Associate Professor with The BioRobotics Institute, Scuola Superiore Sant'Anna, where he leads the Soft Mechatronics for Biorobotics Lab.

He is an author or coauthor of more than 50 international peer-reviewed papers and he regularly serves as a reviewer for more than 25 international ISI journals and for several supporting agencies.

His research interests include bioinspired robotics, soft actuators, smart compliant sensors, and flexible mechanism.